Soft Matter

Multi-scale phase separation in poly(D,L-lactide-co-glycolide) and palmitic acid blends using neutron and X-ray scattering

Journal:	*Soft Matter*
Manuscript ID	SM-ART-11-2024-001367.R1
Article Type:	Paper
Date Submitted by the Author:	07-Feb-2025
Complete List of Authors:	Wolf, Caitlyn; National Institute of Standards and Technology, NIST Center for Neutron Research Dalgliesh, Robert; Rutherford Appleton Laboratory, ISIS Neutron Muon Source, Science and Technology Facilities Council de Campo, Liliana; Australian Nuclear Science and Technology Organisation, Australian Centre for Neutron Scattering Smith, Gregory; Rutherford Appleton Laboratory, ISIS Neutron Muon Source, Science and Technology Facilities Council Weigandt, Katie; National Institute of Standards and Technology, NIST Center for Neutron Research

Multi-scale phase separation in poly(D,L-lactide-*co*-glycolide) and palmitic acid blends using neutron and X-ray scattering

Caitlyn M. Wolf[1,*], Robert M. Dalgliesh[2], Liliana de Campo[3], Gregory N. Smith[2], Katie M. Weigandt[1,*]

[1]NIST Center for Neutron Research, National Institute of Standards and Technology, Gaithersburg, MD 20899, United States

[2]ISIS Neutron Muon Source, Science and Technology Facilities Council, Rutherford Appleton Laboratory, Didcot OX11 0QX, United Kingdom

[3]Australian Centre for Neutron Scattering (ACNS), ANSTO, Lucas Heights, NSW 2234, Australia

**corresponding authors*

**Email:* caitlyn.wolf@nist.gov

**Email:* kathleen.weigandt@nist.gov

Abstract

In this work neutron and X-ray scattering are used to quantitatively characterize multi-scale phase separation in a model blend of poly(D,L-lactide-*co*-glycolide) or poly(D,L-lactide), both synthetic biodegradable polymers, and palmitic acid. We find that phase separation occurs on two different length scales from tens of nanometers to microns. Moreover, the large-scale phase separation mechanism is sensitive to the lactide to glycolide ratio of the polymer matrix and can limit the growth of nanoscale domains of the dispersed palmitic acid. The multiscale structure in these composite materials is directly tied to function in pharmaceutical applications where phase separation and small molecule crystallization are factors that determine controlled release behaviors and drug efficacy.

1. Introduction

Polymer and small molecule formulations are found in a wide variety of applications. Polymers have been used to improve processibility while controlling crystallization of small molecule semiconductors[1]; release antimicrobials, antioxidants, or other active agents from edible or biodegradable coatings[2–5]; template wax recrystallization with a hierarchical structure to mitigate plugging of crude oils and diesel fuels in flow conditions[6]; and to encapsulate or stabilize phase change materials for thermal energy storage applications.[7,8] In all of these systems, molecular interactions between the polymer chains and small molecules influence structure and phase separation, and therefore performance, of the blend. In this study we focus on a specific type of polymer-small molecule blends used in the pharmaceutical industry.

Polymer-based pharmaceutical formulations have a vast design space that provides access to a broad range of functionality, from burst to sustained drug release, oral pills and tablets, to biodegradable or non-biodegradable implants, and this has led to the development of many advanced technologies.[9–15] Forms include solid films, fibers, porous membranes, or injectable self-assembling colloidal systems, such as polymeric nanoparticles or hydrogels.[12–16] In solid blends or composite materials, the active pharmaceutical ingredients (APIs) are dispersed throughout a matrix of one or more polymers and any desired additives, or the polymer chains can be covalently modified with active moieties to form polymer-drug conjugates.[12–14,17] Alternatively, concentrated drug cores are encapsulated by polymer coatings or membranes with a controlled degradation time or desired diffusion rate.[12,13] Amorphous solid dispersions (ASDs) are one type of composite- or blend-type formulation that rely on a polymer matrix to kinetically trap amorphous phases of a poorly-water-soluble API to increase its free energy and bioavailability to the body.[18–21]

Migration, phase separation, and eventual recrystallization of the dispersed API can limit an ASD's shelf-life and efficacy. Therefore, understanding the structure and phase morphology across many length scales, which are sensitive to thermal, chemical, and mechanical conditions during manufacturing, storage, and administration, is important to advancing development of these polymer and small molecule formulations.[21,22] The size, polydispersity, and heterogeneity of API-rich domains are relevant to stability, dissolution or drug release behavior, and bioavailability of ASDs.[20,23–28] Yang, *et al.* found that it was the formation of larger continuous API phases near the surface of the blend in solution that slowed drug release compared to small droplet-like domains of the drug in a binary polymer-drug dispersion.[25] While one or more polymers often make up the bulk of the material, additives such as surfactants or salts can be used to further aid in the dissolution and uptake processes or to slow recrystallization of the drug.[26,29] Saboo and coworkers found that surfactants could be added to a binary polymer-drug ASD to prevent the formation of continuous drug phases at higher drug loadings, improving performance and release across a wider range of compositions.[26]

Meere, *et al.* note that even in binary dispersions, a range of phase separation mechanisms can occur, including Ostwald ripening, droplet coalescence into chains or strings, and phase inversion.[22] Complexity only grows with the inclusion of other polymers, additives, or multiple active ingredients. The most common techniques employed for ASD characterization include differential scanning calorimetry (DSC), solid-state nuclear magnetic resonance (SSNMR), and powder X-ray diffraction (PXRD).[19,30,31] Thermal transitions, including glass transition and melting, molecular relaxations and mobility, and interactions between drug and polymer molecules gathered from DSC and SSNMR combined with the crystalline structure provided by PXRD are used to estimate the amount of crystalline and amorphous material present in ASDs and further

understand the extent of phase separation.[19,31] However, neither method is directly probing domain size of the separated material, and complex or overlapping thermal information can make this analysis difficult.[19,28,30] Polarized optical microscopy, scanning electron microcopy, transmission electron microscopy, and atomic force microscopy often complement these methods but they can be transmission, contrast or surface-limited depending on the atomic composition of the organic materials in the ASDs.[19,30] More recently, X-ray micro-computed tomography (XμCT) has enabled rich tomographic reconstructions of ASD bulk structure and a means to probe uniformity of the material, but the technique relies on differences in electron density for contrast, making it difficult to differentiate between crystalline and amorphous phases of many materials.[27,28,30]

Small angle neutron scattering (SANS) and ultra-small-angle neutron scattering (USANS) provide a complementary characterization approach at length scales from nanometers to tens of microns. Neutrons are not limited to optically transparent materials, provide information about the bulk structure, and enable use of selective deuteration and contrast variation to improve contrast between organic phases with similar elemental compositions. The impact of SANS in polymer research is nothing new but its use in drug-delivery solid dispersions has been minimal.[32,33] In one study, SANS, USANS, and neutron reflectometry enabled Wu, *et al.* to characterize phase separation and drug release in electrospun fibers of PLGA and the active molecule capecitabine as the polymer degraded in buffer solution and released the drug molecules.[32] The team was also able to track growth of the nanoscale drug aggregates and swelling of the matrix polymer on the micron scale under varying humidity, temperature, and buffer conditions.

In this work, SANS, USANS, spin-echo SANS (SESANS), wide-angle X-ray scattering (WAXS), and polarized optical microscopy are used to characterize phase separation and recrystallization in blends of palmitic acid (PA) and a poly(D,L-lactide-*co*-glycolide) (PLGA) or

poly(D,L-lactide) (PDLLA) matrix. PLGA/PDLLA are synthetic amorphous biodegradable polymers found in many existing ASD formulations and other biorelevant technologies.[12,13,15,32,34–36] Their end groups and lactide:glycolide ratio are used to tune degradation time and release of active ingredients.[12,13,35] Palmitic acid has also been used as an additive in solid dispersions and other polymer-based pharmaceutical formulations.[37–41] Understanding how additives interact with the matrix polymer alone without the presence of active ingredients can be useful for tuning structure in more complex formulations. Here we are interested in understanding the multi-scale phase separation and structure in blends of PLGA and palmitic acid as a function of composition, including matrix chemistry and palmitic acid loading concentration. Although these materials were chosen in the context of pharmaceutical formulations, we emphasize that this study is relevant to many other applications using mixtures of polymers and small molecules.

2. Materials and Methods

2.1. PLGA and palmitic acid blends

Resomer RG 502 H, Poly(D,L-lactide-*co*-glycolide) acid terminated, lactide:glycolide 50:50, Mw 7000 g/mol – 17000 g/mol (PLGA 50:50 AT), Resomer RG 752 H, Poly(D,L-lactide-*co*-glycolide) acid terminated, lactide:glycolide 75:25 Mw 4000 g/mol – 15000 g/mol (PLGA 75:25 AT), Resomer R 202 H, Poly(D,L-lactide) acid terminated Mw 10000 g/mol – 18000 g/mol (PLGA 100:0 AT), and Resomer R 202 S, Poly(D,L-lactide) ester terminated Mw 10000 g/mol – 18000 g/mol (PLGA 100:0 ET) were purchased from Millipore Sigma and used as received. These are all amorphous polymers developed for drug-delivery applications, and they were selected from the supplier class targeting similar inherent viscosities of 0.16 dL/g to 0.24 dL/g (RG 752 H designed at 0.14 dL/g - 0.22 dL/g) and similar molecular weights. They are also designed to fully degrade within 3 months (RG 502 H), 6 months (RG 752, R 202 H), and 9

months (R 202 S) in aqueous biorelevant conditions. PLGA 50:50 and PLGA 75:25 polymers are random copolymers of glycolide and lactide (both D and L isomers) monomers at the lactide to glycolide molar ratios of 50:50 and 75:25, respectively. The PLGA 100:0 polymers are random copolymers of the D and L lactide isomers to ensure they remain amorphous. Hexadecanoic-d_{31} acid, $CD_3(CD_2)_{14}COOH$, 98 % D, (palmitic-d_{31} acid, PA-d_{31}) was purchased from CDN Isotopes and used as received. Fully hydrogenated hexadecenoic acid (palmitic acid, $\geq$ 99 %) was purchased from Millipore Sigma and used as received.

Films were prepared using a lab-scale syringe extrusion process. Raw materials of a single selected matrix polymer and mass fractions of 0 % to 25 % of PA-d_{31} were mixed in the solid state then loaded into polypropylene 1 mL lab syringes. For SESANS samples, the contrast was modulated at 10 % and 25 % loadings by blending PA-d_{31} and fully hydrogenated palmitic acid at PA-d_{31} mass fractions of 79 % and 65 %, respectively, to prevent a full loss of polarization. The loaded syringes were placed in an oven set at maximum 130 °C to prevent softening of the syringe. After initial melting for 30 minutes, a slight vacuum was pulled for an additional 90 minutes to encourage removal of air bubbles trapped in the molten blend. The samples were then plunged from the syringe onto a glass slide covered with Kapton film on top of a hot plate set at 100 °C and inside an aluminum washer with a thickness of 0.5 mm. An additional piece of Kapton film and glass slide were then used to press the sample in the washer. The washer provided a mold in which to press films to a thickness of 0.5 mm. The washer also served as a sample frame or holder during measurements. After pressing, the samples were placed on the lab bench to rapidly quench them to room temperature. All subsequent measurements were taken at ambient temperature of approximately 20 °C.

2.2. Small-angle neutron scattering (SANS)

SANS measurements were made on Bilby[42,43] at the Australian Centre for Neutron Scattering (ACNS) at Australian Nuclear Science and Technology Organisation (ANSTO). Bilby was configured in time-of-flight mode with wavelengths between 3.0 Å to 18.0 Å. The Mantid software[44] was used to reduce the data and is described in Sokolova *et al.*[43]. A circular aperture with a size of 12.5 mm was used for all measurements. The samples were aged 6 months at the time of the SANS measurements. For samples with a PA-d_{31} mass fraction of 10 % or higher, the data was trimmed to only include wavelengths from 3.0 Å to 13.0 Å to minimize multiple scattering effects at the lowest *q*-values. The scattering contribution from the matrix phase, which could include either random density fluctuations of the quenched amorphous material or air bubbles, was subtracted from the scattering spectra for the blends.

2.3. Ultra-small-angle neutron scattering (USANS)

USANS measurements were made on Kookaburra[45] at ACNS at ANSTO with a wavelength of 4.74 Å and a slit length of 0.0586 $Å^{-1}$. A circular aperture with a size of 12 mm was used for all measurements. The data was reduced using adapted Python scripts in Gumtree[46] based on the NCNR USANS reduction macros[47]. The sample were aged 6 months at the time of the USANS measurements. Some of the samples were wrapped in Kapton tape for improved stability of the film during measurements. A background measurement of the Kapton tape used did not show measurable scattering above an empty background. The slit-smeared USANS data was analyzed directly with slit-smeared models rather than applying a desmearing algorithm to the data.

2.4. Spin-echo small-angle neutron scattering (SESANS)

SESANS measurements were made on Larmor at the ISIS Neutron and Muon Source at Rutherford Appleton Laboratory at a 1.0 MHz frequency, wavelengths between 3 Å and 9 Å, and

pole shoe angles of 60°, 75°, and 88°. Here, the pole shoe angle is defined as the inclination of the magnetic field with respect to the direction of the neutron beam. The Mantid software[44] with the monitor correction described in Li, *et al*.[48] was used to reduce the data, and the raw data is available via the ISIS data repository[49]. All samples were aged 1 month at the time of the SESANS measurements and were wrapped in Kapton tape for improved stability of the film. A background measurement of the Kapton tape used showed no appreciable scattering above an empty background and was subtracted from the sample data during reduction.

2.5. Wide-angle X-ray scattering (WAXS)

WAXS measurements were performed on a Xenocs Xeuss SAXS/WAXS instrument with a 300K Pilatus detector and a copper source with a wavelength of 1.54 Å. The X-ray beam size was 0.8 mm in diameter. All measurements were performed at an ambient temperature of approximately 20 °C. Data reduction, including background subtraction and integration from 2D images to 1D spectra, was performed using the Nika Igor macro.[50] Samples were held between two pieces of Kapton tape for loading on the solid sample holder. Measurements were taken at five different locations across the sample. All samples were aged 15 months at the time of measurements.

2.6. Polarized optical microscopy

Transmission polarized optical microscopy was performed on an Olympus BX51 instrument at a magnification of 50x. A 530 nm lambda plate was used for the measurement. Kapton tape was removed from all samples and the films were then loaded onto microscope slides for imaging. This plate results in a magenta color in isotropic regions and a variety of colors (depending on orientation) in birefringent regions. All samples were aged 17 months at the time of measurements.

3. Results & Discussion

Figure 1 shows SANS and USANS data for blends of PLGA at varying lactide:glycolide ratios and mass fractions of palmitic acid loading from 5 % to 25 %. The most obvious feature in these plots is the mismatch between the low q (USANS) and high q (SANS) data, which is due to instrumental resolution and not related to the structure of the sample. The USANS instrument utilizes a quintuple crystal monochromator that leads to a highly collimated beam in the horizontal direction and a poorly collimated beam in the vertical direction. This "slit-smearing" of the USANS data results in an disconnect between the USANS spectra and SANS spectra which is collimated with a circular aperture with "pinhole" smearing. While desmearing algorithms are sometimes used to reconnect this data, this introduces significant noise to the USANS data, and it is more advantageous to include resolution in the models used to analyze the data to account for this effect without introducing additional error.

From Figure 1 the SANS and USANS data are capturing structural changes occurring at two different length scales, orders of magnitude apart, in the PLGA and palmitic acid blends as a function of both the matrix polymer and palmitic acid concentration. In all four matrix polymer composites there are two key features: a knee in the high q (between 0.01 $Å^{-1}$ and 0.1 A^{-1}) and a turnover in the low q (between 10^{-3} $Å^{-1}$ and 10^{-4} $Å^{-1}$). Furthermore, in some concentration series the total scattering increases with larger loadings of palmitic acid which reflects an overall increase in volume fraction of palmitic acid domains in the sample.

In the high q there are clear changes in the location and shape of the SANS curves as a function of matrix composition and palmitic acid loading. We attribute these small domains to either recrystallized or micellar palmitic acid trapped in the PLGA matrix. Similar small domains of the drug molecules were also observed in Wu, *et al.* Fortunately, in the high-q we can quantify

changes in the shape of the knee region as well as volume fraction of palmitic acid domains with increased loading using sphere or ellipsoid form factors. An assumption is made that the contrast is equal to that between PA-d_{31} and PLGA. We note that this assumption does not yet account for PA-d_{31} chains trapped within the polymer matrix phase but we can still learn information about the effects of sample composition on these small domains. To apply the sphere or ellipsoid form factor fit to the knee feature, the knee had to be isolated from the scattering arising from larger structures that give rise to the low q features. This was achieved by fitting a combined power law[51] and sphere model[52] or combined power law [51] and ellipsoid model[53] to the SANS data. The power law model fit the slope at lower *q* values and accounted for the scattering from larger structures while the sphere or ellipsoid model fit the knee feature in the SANS data. The ellipsoid model as implemented in SasView calculates the small angle scattering from randomly oriented ellipsoids of revolution where two radial dimensions are equal to the equatorial radius and one radial dimension is equal to the polar radius.[51,53] These combined fits are showed overlaid on the data in Figures S1-S4 of the supplementary information.

From this analysis we determine the volume fraction and size of the small palmitic acid domains. The volume fractions are plotted in Figure 2. For acid-terminated PLGA matrices, the volume fraction of small domains is inversely related to glycolide concentration, apart from an outlier in the PLGA 75:25 system at a 5 % loading. For matrices containing glycolide, the volume fraction of the small domain changed only minimally with concentration of palmitic acid. We observed a significant increase in the concentration of small domains with small molecule concentration in the acid-terminated matrix with 100 % lactide groups (PLGA 100:0 AT). The volume fraction of small domains in the PLGA 100:0 ester-terminated matrix was consistent across all palmitic acid concentrations, and it was nearly 4x higher than the glycolide-containing acid-

terminated matrix polymers. The corresponding sphere and ellipsoid radii from these fits are provided in Table 1. In the blends comprised of an acid-terminated matrix, we observe an increasing diameter with increased glycolide units. The largest difference is observed at a loading of 5 % where the domains in a matrix of PLGA 50:50 have a diameter 1.8x that of the domains formed in the PLGA 100:0 matrix. The knee feature of blends with a glycolide-containing matrix showed a single slope change and could all be fit with a sphere model. For PLGA 100:0 AT, a sphere model could be used in blends with a 5 % or 10 % loading but an ellipsoid model was required at a 25 % loading to capture two observed slope changes in the knee feature. This sample required a polar radius slightly smaller than the sphere radius at 5 % and 10 %, but the equatorial radius was approximately 2.6x the sphere radii. An ellipsoid model was required for all samples with an ester-terminated PLGA 100:0 matrix. Both the polar and equatorial radii remained approximately constant with increased loading of palmitic acid, similar to the trend observed for the volume fraction of the same samples, with an equatorial radius 3x to 4x larger than the polar radius. At all loadings, the small domains were larger than those in the blends with an acid-terminated PLGA 100:0 matrix. These results indicate that both interactions between the palmitic acid and the lactide or glycolide groups as well as interactions with the end groups affect the size of these palmitic acid domains trapped in the matrix.

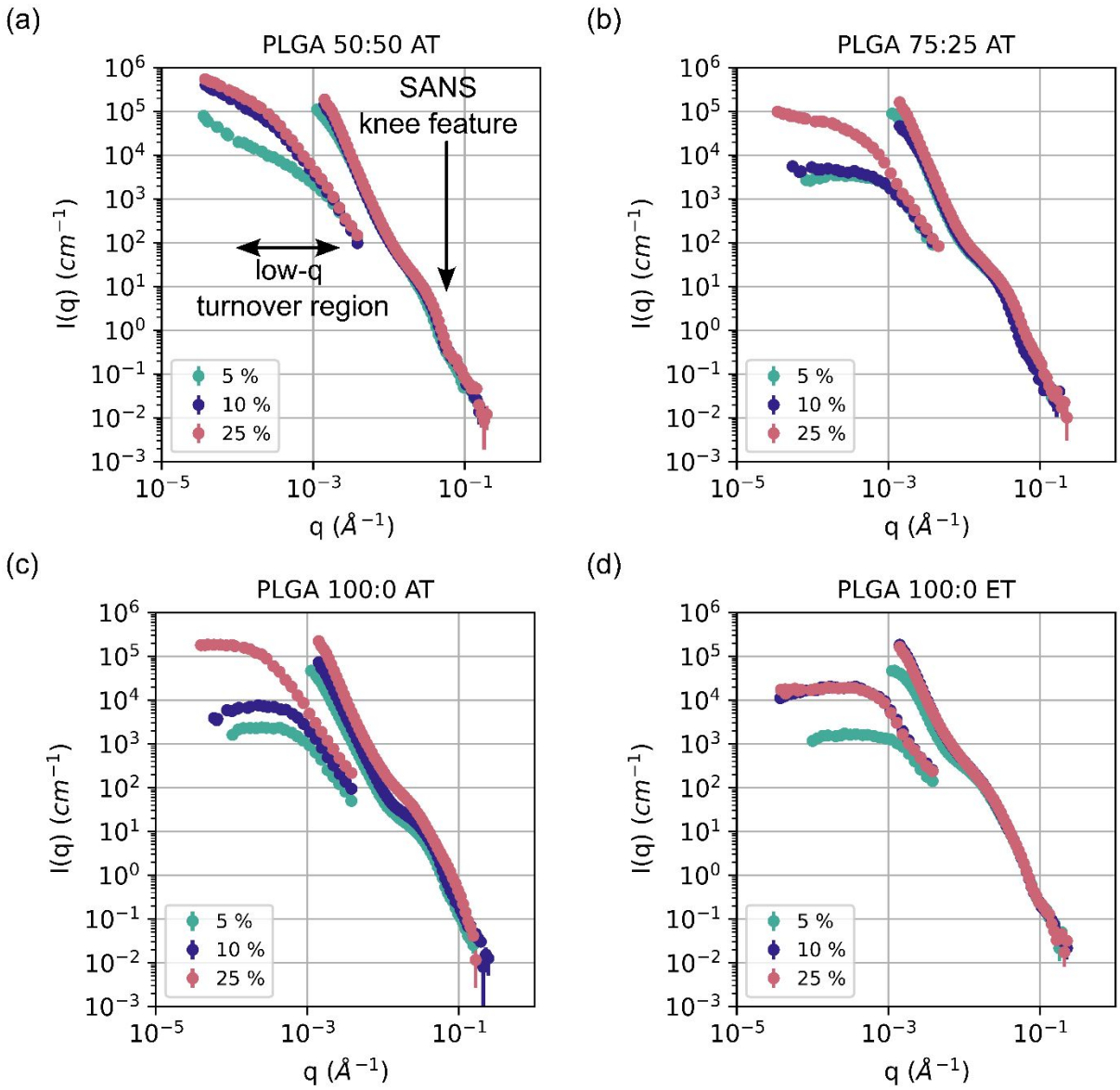

Figure 1. SANS and slit-smeared USANS data for blends comprised of an (a, b, c) acid-terminated or (d) ester-terminated PLGA matrix at varying lactide:glycolide ratios of 50:50, 75:25, or 100:0 with dispersed palmitic-d31 acid at nominal mass fractions from 5 % to 25 %. Error bars represent standard errors and may be smaller than the marker size.

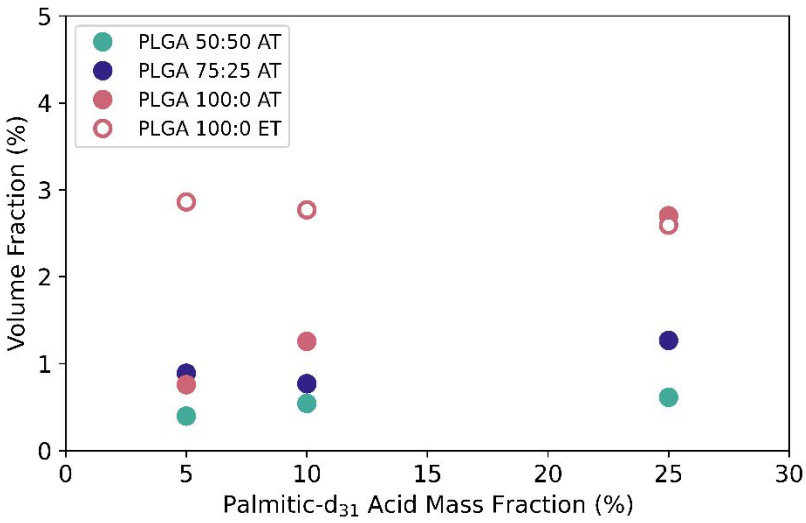

Figure 2. Volume fraction from sphere or ellipsoid model fits to knee feature of SANS data shown in Figure 1 for blends comprised of an acid-terminated or ester-terminated PLGA matrix at varying lactide:glycolide ratios of 50:50, 75:25, or 100:0 with dispersed palmitic-d_{31} acid at nominal mass fractions from 5 % to 25 %. Error bars correspond to the standard error of the scale term provided by the fitting algorithm and are smaller than the marker size.

Table 1. Radii from sphere or ellipsoid model fits to knee feature of SANS data shown in Figure 1 for blends comprised of an acid-terminated or ester-terminated PLGA matrix at varying lactide:glycolide ratios of 50:50, 75:25, or 100:0 with dispersed palmitic-d_{31} acid at nominal mass fractions from 5 % to 25 %.

Matrix Polymer	Total Mass Fraction of Palmitic Acid	Sphere Radius[1]	Ellipsoid Polar Radius[1]	Ellipsoid Equatorial Radius[1]
PLGA 50:50 AT	5 %	8.10 nm ± 0.03 nm (25 %)		
	10 %	7.27 nm ± 0.02 nm (20 %)		
	25 %	6.79 nm ± 0.02 nm (20 %)		
PLGA 75:25 AT	5 %	6.57 nm ± 0.02 nm (20 %)		
	10 %	7.27 nm ± 0.02 nm (20 %)		
	25 %	5.208 nm ± 0.009 nm (30 %)		
PLGA 100:0 AT	5 %	4.53 nm ± 0.01 nm (30 %)		
	10 %	4.46 nm ± 0.008 nm (30 %)		
	25 %		2.61 nm ± 0.01 nm (20 %)	11.77 nm ± 0.05 nm (0 %)
PLGA 100:0 ET	5 %		4.14 nm ± 001 nm (20 %)	16.86 nm ± 0.05 nm (0 %)
	10 %		4.55 nm ± 0.01 nm (10 %)	15.96 nm ± 0.06 nm (20 %)
	25 %		4.55 nm ± 0.02 nm (10 %)	15.00 nm ± 0.07 nm (20 %)

[1]Errors correspond to standard error from fitting algorithm. Polydispersity is provided in parentheses and is defined as the standard deviation of a Gaussian distribution divided by the mean (fit radius).

In the USANS data, clear structural changes are observed when comparing blends with different PLGA lactide:glycolide ratios and palmitic acid concentration. In blends with a PLGA matrix comprised of only lactide groups, i.e., PLGA 100:0, with either an acid or ester end group shown in Figure 1(c, d), a turnover into the Guinier plateau occurs between 0.0001 $Å^{-1}$ and 0.001 $Å^{-1}$. A similar turnover occurs for the blends comprised of both lactide and glycolide groups, i.e., PLGA 50:50 and PLGA 75:25; however, for the highest concentration of palmitic acid in PLGA 75:25 (Figure 1(b)) we start to observe a continuously increasing slope beyond 0.0001 $Å^{-1}$. For the blend containing equal parts lactide and glycolide groups (Figure 1(a)) a slope change is still observed, but instead of transitioning to a slope of 0 (a Guinier plateau) a slope of one is observed. When correcting for instrumental smearing, a power law of q^{-2} exists indicating large two-dimensional domains beyond the length scales resolved with USANS. These turnovers and their associated structure also grow with increased palmitic acid loading as indicated by a shift in the turnover location to lower q-values. A variety of models, including polydisperse sphere or ellipsoid form factors, were attempted to be fit to the USANS data, but failed to capture these structural features in the turnover region. The small-angle scattering transmission, T_{SAS}, from the USANS measurements reached as low as 46 %, with the lowest values occurring for blends with a palmitic acid loading of 10 % or higher. At T_{SAS} values less than 90 %, multiple scattering is likely to have a significant effect on the data.[54] Even some samples with only a 5 % loading of the palmitic acid were below this threshold. Therefore, these structural features in the USANS data would be broadened due to the multiple scattering effects. This makes fitting to the standard form factors and structure factors difficult without accounting for the multiple scattering in our model.

To better understand the origin of large-scale structural features present in the USANS data, polarized optical microscopy was used to image the blends at the micron to macro scales.

The small nanoscale domains captured in the SANS spectra were below the diffraction limit of the microscope. Contrast between the matrix and palmitic acid arises due to birefringence in the crystalline domains of the small molecule. The microscopy images are shown Figure 3 for blends comprised of an acid-terminated PLGA matrix with lactide:glycolide ratios of 50:50 and 100:0 at mass fractions of palmitic acid of 0 %, 5 %, and 10 %. Samples at a palmitic acid concentration of 10 % were difficult to image due to the opaque white color of the recrystallized palmitic acid domains. This resulted in cloudy images. Samples at palmitic acid concentrations of 25 % were impossible to image. In blends with a PLGA 50:50 matrix, large ellipsoidal domains of recrystallized PA-d_{31} are observed at multiple orders of magnitude in size. This would lead to the slope changes observed in the USANS data for blends with a matrix of PLGA 50:50. In blends with a PLGA 100:0 matrix, a co-continuous droplet or chaining structure appear with a correlation length of approximately 1 μm to 3 μm, and no large crystalline domains could be found. This structure is better seen in the enlarged images provided in Figure 4. The presence of these correlation length domains cannot be seen in the matrix control sample in the absence of palmitic acid. It is possible that random copolymer fluctuations of the two enantiomers of PLGA 100:0 (PDLLA) are present.[55,56] An alternative explanation is that the palmitic acid could be inducing this phase separation. In either case, the presence of these two, almost equal, domains and the lack of large crystalline deposits of pure palmitic acid indicate that these blends are phase separating into two domains that are rich and poor in palmitic acid.

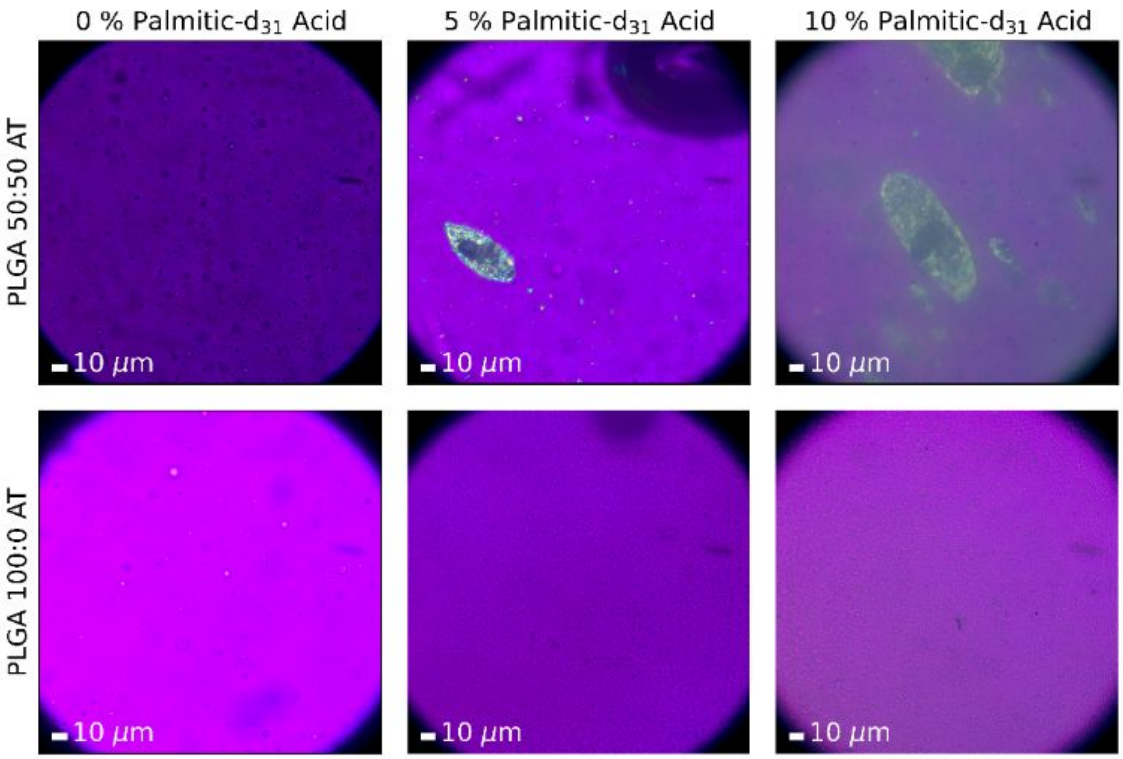

Figure 3. Polarized optical microscopy images of blends comprised of an acid terminated PLGA matrix at varying lactide:glycolide ratios of 50:50 (top row) or 100:0 (bottom row) with dispersed palmitic-d31 acid at mass fractions of 0 %, 5 % and 10 %.

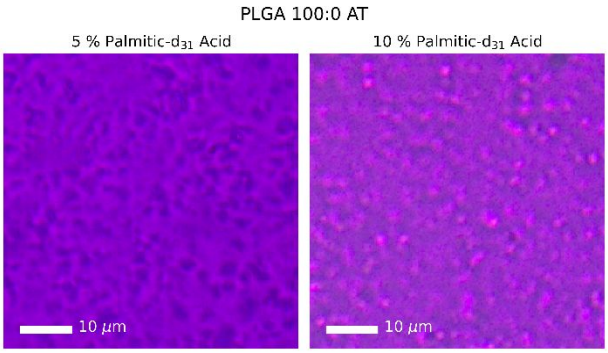

Figure 4. Polarized optical microscopy images of blends comprised of an acid-terminated PLGA matrix at a lactide:glycolide ratio of 100:0 with dispersed palmitic-d31 acid at mass fractions of 5 % (left) and 10 % (right).

To better quantify the observations noted from the polarized microscopy and USANS, SESANS was an ideal technique as the multiple scattering that made the USANS data challenging to model is naturally accounted for in SESANS measurements. For this reason, SESANS was used to quantitatively characterize these large-scale phase separation mechanisms at the higher concentrations of palmitic acid. SANS and SESANS data are related, for isotropic scattering, through the Hankel transform[57–59] and to slit-smeared USANS data through a Fourier cosine transform.[60] This close relationship and numerical implementation of the Hankel transform in SasView means that many of the same models originally developed for SANS can be fit to SESANS data. Figure 5 shows SESANS results for samples comprised of PLGA matrixes at varying lactide:glycolide ratios and palmitic acid loading between 5 % and 25 %. A greater loss in polarization (more negative values) indicates the presence of more small-angle scattering in the sample. Like SANS and USANS, slope changes or turnovers are indicative of structural changes at that correlation length. However, SESANS is most sensitive to large structures and a strong coherent scattering cross section (higher contrast, concentration, etc.) which made measurement

of blends with low concentrations of palmitic acid difficult with this technique. Moreover, sample thickness could not be increased to improve signal due to the large amount of incoherent scattering arising from the protonated matrix polymer. This reduces the transmitted signal and increases multiple and wide-angle scattering to such an extent that the multiple scattering formalism of SESANS is no longer applicable.

In the SESANS data for samples with a PLGA 50:50 matrix and palmitic acid loading of 10 % and 25 % (Figure 5(a)), a gradual slope change occurs between a few hundred nanometers and 1 μm. After this feature, there is a continuing loss in polarization that indicates the presence of structural features beyond the resolvable length scales. In the spectra for samples with a PLGA 75:25 matrix (Figure 5(b)), a similar trend is observed for the 25 % loading, but with a more gradual slope, and a plateau is observed for the 10 % loading. These results are consistent with the respective USANS data. The SESANS data for acid-terminated and ester-terminated PLGA 100:0 samples (Figure 5(c, d)) display a different feature. Between 1 μm and 3 μm a dip or trough is observed followed by a rise in the spectra for some of the spectra. This indicates long range order of a repeated correlation length and can be modeled with a structure factor. The analogous feature was not observable in the USANS data due to multiple scattering; however, this feature is consistent with polarized optical microscopy where a co-continuous structure of two phases was observed.

Based on the polarized microscopy, a polydisperse ellipsoidal form factor was used to fit the SESANS data for glycolide containing samples (PLGA 50:50 AT and PLGA 75:25 AT). We assume that the ellipsoid composition is pure crystalized palmitic acid surrounded by matrix polymer due to the birefringence observed in the microscopy images. All parameters from the fits are provided in the supplementary information. Because the largest length scales are not

resolvable, the polar radius was fixed to 20 μm (beyond the resolvable length scale range, but consistent with the large ellipsoids observed in the polarized microscopy). The equatorial radius was allowed to vary enabling a good fit of the turnover feature. The results of equatorial radius and ellipsoid volume fraction are provided in Table 2. The ellipsoidal domains become larger with increasing palmitic acid and glycolide content. The volume fraction of the ellipsoidal domains also increases with higher palmitic acid loading, but determining concentration also requires knowledge of the contrast. In our fits of the ellipsoid model, we assume the matrix is pure PLGA. This does not account for the small domains (where a contrast assumption is also made) nor any trapped chains of the palmitic acid in the polymer. Therefore, the concentration is likely underestimated and could be up to 25 % to 90 % higher for samples at palmitic acid mass fractions of 10 % and 25 %, respectively, after accounting for the mass balance.

Based on the polarized microscopy, a spinodal model was selected to fit to the correlation length scale observed in the SESANS spectra for the matrix polymers containing 100 % lactide (PLGA 100:0 AT and ET). The spinodal model in SasView calculates the structure factor that arises due to co-continuous phases with a single correlation length that are formed during spinodal decomposition of two materials.[51,61–63] In this work we use this model to extract the correlation length of these domains. This length scale is calculated as $\frac{2\pi}{q_0}$ where q_0 is the location of the structure factor peak in the small-angle scattering spectra $I(q)$. This corresponds to the dip and oscillation observed in the SESANS data. All parameters from the fits are provided in the supplementary information and the correlation lengths are provided in Table 3 of the main manuscript. At a 25 % palmitic acid loading in the acid-terminated blends and at 10 % and 25 % palmitic acid loadings in the ester-terminated blends, the blends form co-continuous phases with correlation lengths between 2.5 μm and 3.1 μm. The strong signal and contrast between these

domains in our neutron measurements confirms the microscopy results that the palmitic acid is favoring one of these two phases.

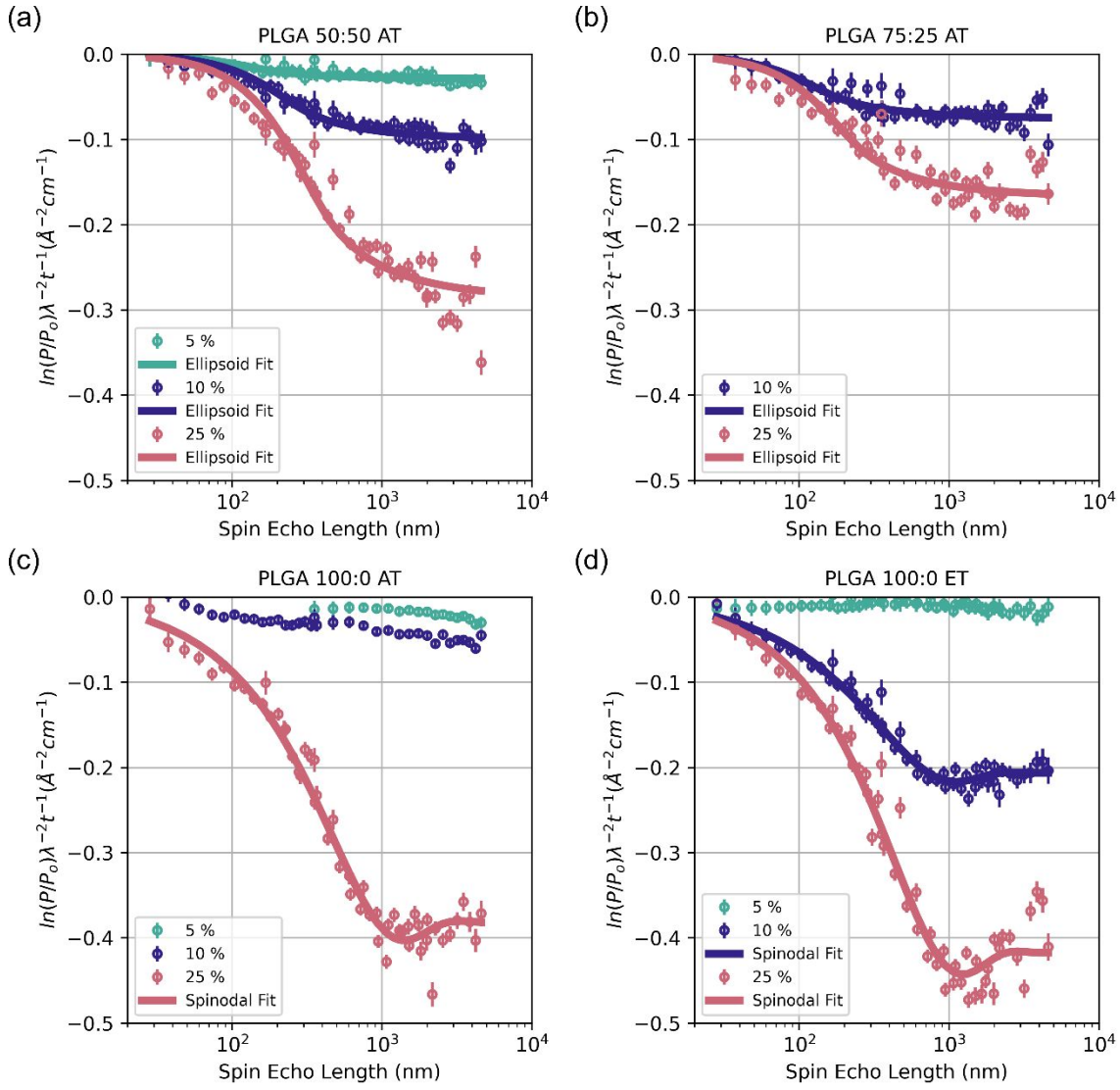

Figure 5. SESANS data for blends comprised of an (a, b, c) acid-terminated or (d) ester-terminated PLGA matrix at varying lactide:glycolide ratios of 50:50, 75:25, or 100:0 with dispersed palmitic acid at nominal mass fractions from 5 % to 25 %. All samples were quenched and aged 1 month prior to measurement. Contrast at 10 % and 25 % palmitic acid was modulated by blending palmitic acid-d31 with fully hydrogenated palmitic acid. Data has been scaled assuming full contrast (palmitic-d31 acid only and PLGA) for visual comparisons of across different samples and measurements.

Table 2. Equatorial radii and volume fraction extracted from fits of a polydisperse ellipsoidal model to SESANS data shown in Figure 5(a, b) of the main manuscript. Blends are comprised of an acid-terminated PLGA matrix with a lactide:glycolide ratio of 50:50 or 75:25 and dispersed palmitic acid at mass fractions from 5 % to 25 %. Polar radius was held constant at 20 μm.

Matrix Polymer	**Mass Fraction of Palmitic Acid**	**Equatorial Radius[1]**	**Volume Fraction[1]**
PLGA 50:50 AT	10 %	155 nm ± 18 nm	1.2 % ± 0.1 %
	25 %	217 nm ± 18 nm	2.5 % ± 0.2 %
PLGA 75:25 AT	10 %	88 nm ± 15 nm	1.4 % ± 0.2 %
	25 %	129 nm ± 19 nm	2.1 % ± 0.3 %

[1]Errors correspond to standard deviations from the fitting algorithm.

Table 3. Correlation distances extracted from fits of the spinodal model to SESANS data shown in Figure 5(c, d) of the main manuscript. Blends are comprised of a PLGA matrix at a lactide:glycolide ratio of 100:0 with dispersed palmitic acid at mass fractions from 5 % to 25 %.

Matrix Polymer	**Mass Fraction of Palmitic Acid**	**Correlation Distance (μm) ± Standard Deviation from Fit (μm)**
PLGA 100:0 AT	25 %	3.1 ± 0.3
PLGA 100:0 ET	10 %	2.5 ± 0.3
	25 %	2.7 ± 0.3

WAXS was then used to better understand the effects of these two different large-scale phase separation modes on the overall recrystallization of the dispersed small molecule in these

blends. The WAXS spectra is shown in Figure 6 for blends comprised of an acid terminated PLGA matrix at lactide:glycolide ratios of 50:50 and 100:0 and PA-d_{31} mass fractions of 5 %, 10 %, and 25 %. Broad Gaussian peaks correspond to amorphous domains while sharper peaks correspond to crystalline domains. For each sample, data was collected at five different locations across the surface of the film, and these spectra are shown with different marker colors in each plot of Figure 6. In many of our samples these measured spectra do not overlap with one another, indicating a degree of heterogeneity in structure and composition across the blend. The large peak at a q value of 0.42 $Å^{-1}$ corresponds to the Kapton tape sample holder, and all spectra were normalized to this peak to enable comparison of the relative concentrations of crystalline domains between samples. The largest broad peak just above a q value of 1 $Å^{-1}$ arises from the amorphous polymer matrix. Finally, the sharp crystalline peaks only appear and grow with increasing palmitic acid concentration and are attributed to recrystallized domains of the small molecule. These are marked with red arrows in Figure 6(e).

The relative contributions of the Kapton holder, PLGA matrix and recrystallized palmitic acid are quantified by fitting a model comprised of multiple Gaussians to each domain and calculating the area under the respective curves. This fit is shown as a solid black line overlaid on the measured data for all samples. More information about this fitting procedure is provided in the supplementary information. The Gaussian peaks fit to the crystalline domains of palmitic acid are shown as blue lines below the WAXS spectra. These are used to estimate the relative volume fraction of recrystallized material by comparing the area under these curves to the area under the full combined model and enable a qualitative examination of the effects of sample composition on recrystallization. The results are provided in Table 4 and they show a similar trend of increasing crystalline material at higher palmitic acid loadings in both PLGA 50:50 and PLGA 100:0

samples. Since the model fits to the SANS spectra results showed a low volume fraction of the small domains in the PLGA 50:50 AT samples, these results indicate that unfavorable interactions between the palmitic acid and glycolide moieties limit the loading of palmitic acid into the polymer matrix and result in large crystalline ellipsoidal deposits of the small molecule. The model fits results showed a higher volume fraction of the small domains in samples with no glycolide units (PLGA 100:0). Since no large crystalline deposits were observed in the microscopy data, the crystalline palmitic acid is only located in a high number of these small domains dispersed through the matrix comprised of domains rich and poor in trapped palmitic acid for a co-continuous morphology.

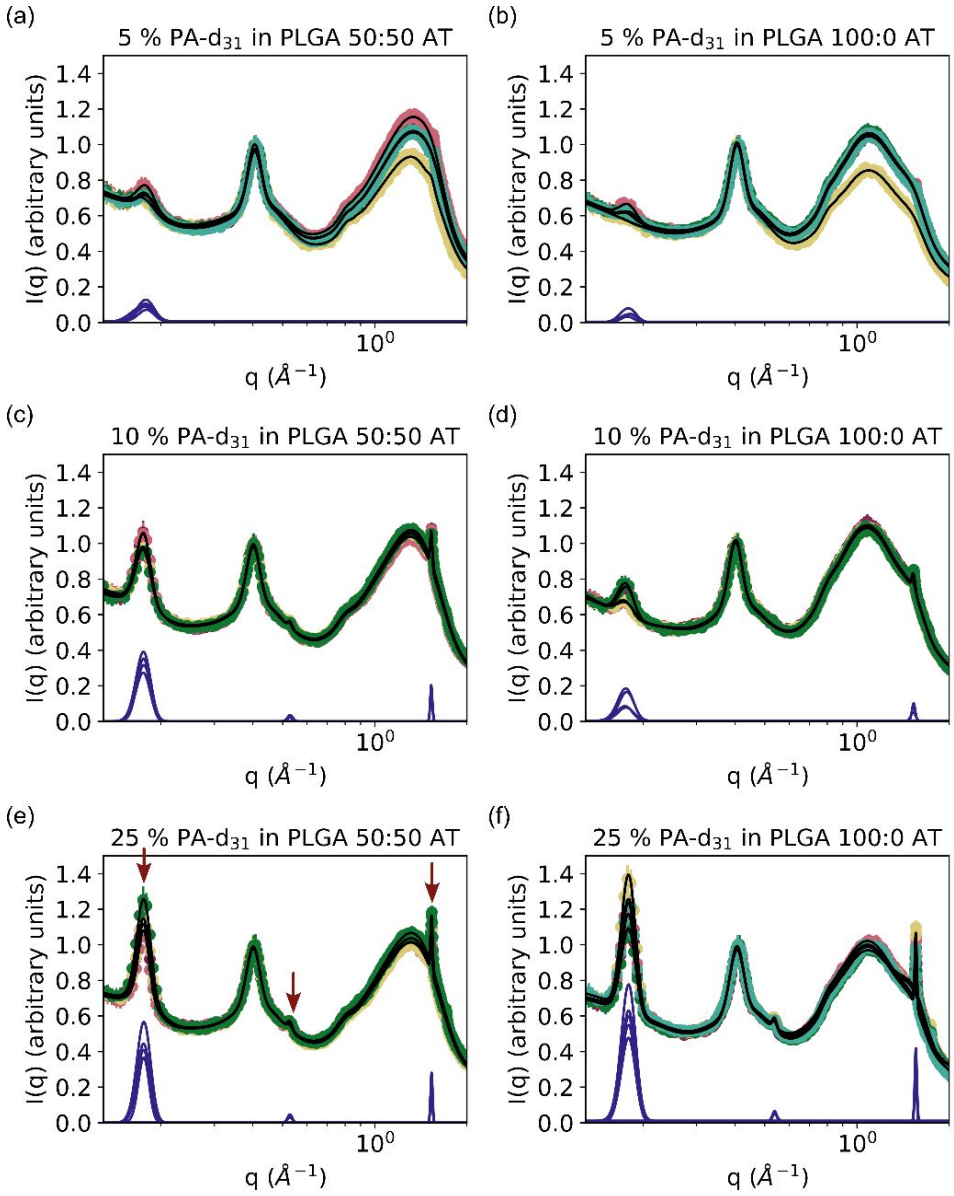

Figure 6. WAXS data for blends comprised of an acid-terminated PLGA matrix at a lactide:glycolide ratio of (a, c, e) 50:50 or (b, d, f) 100:0 and mass fractions of palmitic-d_{31} acid at (a, b) 5 %, (c, d) 10 %, and (e, f) 25 %. Measured data is shown as markers and replicate spectra were collected at multiple locations around the sample. Solid black lines show multi-Gaussian fits to the spectra. Blue solid lines show individual Gaussian fits to the crystalline peaks of palmitic acid used to determine the volume fraction of recrystallized material in the sample.

Table 4. Volume fractions of total crystalline material in blends of PLGA at lactide:glycolide ratios of 50:50 and 100:0 at palmitic acid mass fractions from 5 % to 25 %. Total volume fraction of crystalline material was extracted from fits to WAXS data and error bars correspond to standard uncertainty from multiple measurement locations across the sample.

Matrix Polymer	Mass Fraction of Palmitic Acid	Total Crystalline Volume Fraction
PLGA 50:50 AT	5 %	0.31 % ± 0.08 %
	10 %	1.6 % ± 0.2 %
	25 %	2.0 % ± 0.3 %
PLGA 100:0 AT	5 %	0.12 % ± 0.09 %
	10 %	0.7 % ± 0.3 %
	25 %	2.7 % ± 0.9 %

4. Conclusions

With SANS, USANS, SESANS, WAXS, and microscopy combined we can understand the multi-scale phase separation behavior in blends of PLGA and palmitic acid. All polymer compositions contain small (5 nm – 20 nm) recrystallized or micellar domains of palmitic acid trapped within the matrix. A sphere or ellipsoid model fit of this feature shows that a lower concentration of these small domains is found in blends with glycolide units in the polymer matrix. Large (100 nm – 5 μm) ellipsoidal deposits of pure recrystallized palmitic acid are observed in microscopy images and quantified with SESANS data for these same blends (PLGA 50:50 and PLGA 75:25). Moreover, the volume fraction of these ellipsoidal domains is comparable to the

total volume fraction of crystalline material palmitic acid estimated from the WAXS data. These results indicate that less favorable interactions between the palmitic acid and glycolide moieties limit loading of the small molecule into the PLGA matrix and leave the large crystalline deposits. These large domains of the dispersed small molecule could slow drug release in ASD applications. An example of this can be seen in the previously discussed work of Yang, *et al.* in which researchers found that large API domains slowed drug release when compared to a more continuous structure with dispersed small API droplets.[25]

For polymers containing only lactide monomers (PLGA 100:0), a co-continuous droplet or chaining phase separation into palmitic acid rich and poor domains at relatively large length scales (~3 μm) is observed with polarized microscopy and quantified with the SESANS data. No large deposits of crystalline palmitic acid were observed in the microscopy images, and so the crystalline material measured with WAXS is primarily located in the small nanoscale domains dispersed throughout the matrix. The kinetically trapped co-continuous structure more effectively traps these small domains of recrystallized palmitic acid, preventing significant growth and aggregation. Any growth results in elongated domains captured by the shift from a sphere to ellipsoid shape at higher loadings of palmitic acid. In ester-terminated PLGA 100:0 blends, these domains are ellipsoidal at all loadings of palmitic acid.

Across all applications of polymer and small molecule blends, either of these observed phase separation modes could be chosen to tune the system for a desired functionality. In systems where crystallinity is a useful property of the small molecule, e.g., semiconductors, the large, recrystallized domain structure found in the blends with a glycolide-containing matrix could be selected. In applications where domain size of recrystallized material must be kept small, e.g. ASDs, the large-scale co-continuous structure in blends without glycolide in the matrix could

provide the means to limit growth of the smaller, phase-separated, and recrystallized domains of the small molecule. This emphasizes the importance of understanding the structure and the effects of molecular interactions in these complex materials at many length scales. Future work will aim to understand the effects of thermal processing and aging conditions on these observed structures in PLGA and palmitic acid blends. These results could be useful to designing specific and more complex formulations that control migration, recrystallization, and growth of nanoscale domains of active small molecules by use of large loadings of additives, such as palmitic acid.

5. Conflicts of Interest

There are no conflicts to declare.

6. Data Availability

Raw SESANS data is available at: https://doi.org/10.5286/ISIS.E.RB2220100. Reduced scattering data is available as supplementary information.

7. Acknowledgements

We thank both Jon Seppala and Yimin Mao for their assistance, advice, and helpful discussion during microscopy and wide-angle X-ray scattering measurements, respectively.

This work was supported by National Institute of Standards and Technology (NIST) funding. CMW was supported in part by an appointment to the NRC Research Associateship Program at NIST, administered by the Fellowships Office of the National Academies of Sciences, Engineering, and Medicine. We acknowledge the support of the Australian Centre for Neutron Scattering, ANSTO and the Australian Government through the National Collaborative Research Infrastructure Strategy, in supporting a part of the neutron research infrastructure used in this work via ACNS proposals 14190 and 16792. We acknowledge the ISIS Neutron and Muon Source of Rutherford Appleton Laboratory for the beamtime allocation on Larmor under proposal number RB2220100. This work benefited from the use of the SasView application, originally developed under NSF award DMR-0520547. SasView contains code developed with funding from the European Union's Horizon 2020 research and innovation programme under the SINE2020 project,

grant agreement No. 654000. The Xenocs Xeuss SAXS instrument was purchased as part of NSF award number 1228957.

Certain commercial equipment or software are identified in this paper to foster understanding. Such identification does not imply recommendation or endorsement by the National Institute of Standards and Technology, nor does it imply that the equipment or software identified are necessarily the best available for the purpose.

8. Supplementary Information: Detailed protocol for model fits to the SANS spectra, model parameters from fits to SESANS data, and detailed protocol of WAXS analysis.

9. References

1 L.-H. Chou, Y. Na, C.-H. Park, M. S. Park, I. Osaka, F. S. Kim and C.-L. Liu, *Polymer (Guildf)*, 2020, **191**, 122208.

2 V. M. Rangaraj, K. Rambabu, F. Banat and V. Mittal, *Food Biosci*, 2021, **43**, 101251.

3 M. Zambrano-Zaragoza, R. González-Reza, N. Mendoza-Muñoz, V. Miranda-Linares, T. Bernal-Couoh, S. Mendoza-Elvira and D. Quintanar-Guerrero, *Int J Mol Sci*, 2018, **19**, 705.

4 C. Gomes, R. G. Moreira and E. Castell-Perez, *J Food Sci*, DOI:10.1111/j.1750-3841.2010.01985.x.

5 M. Van Aardt, S. E. Duncan, J. E. Marcy, T. E. Long, S. F. O'Keefe and S. R. Sims, *Int J Food Sci Technol*, 2007, **42**, 1327–1337.

6 A. Radulescu, D. Schwahn, J. Stellbrink, E. Kentzinger, M. Heiderich, D. Richter and L. J. Fetters, *Macromolecules*, 2006, **39**, 6142–6151.

7 M. M. Umair, Y. Zhang, K. Iqbal, S. Zhang and B. Tang, *Appl Energy*, 2019, **235**, 846–873.

8 M. Fashandi and S. N. Leung, *Mater Renew Sustain Energy*, 2017, **6**, 14.

9 S. Shakibania, M. Khakbiz and P. Zahedi, *Soft Matter*, 2023, **19**, 3147–3161.

10 H. Huang, Y. Lyu and K. Nan, *Soft Matter*, 2023, **19**, 1269–1281.

11 P. W. Lee, S. Shukla, J. D. Wallat, C. Danda, N. F. Steinmetz, J. Maia and J. K. Pokorski, *ACS Nano*, 2017, **11**, 8777–8789.

12 N. N. Nyamweya, *Futur J Pharm Sci*, 2021, **7**, 18.

13 S. Borandeh, B. van Bochove, A. Teotia and J. Seppälä, *Adv Drug Deliv Rev*, 2021, **173**, 349–373.

14 I. R. Calori, G. Braga, P. da C. C. de Jesus, H. Bi and A. C. Tedesco, *Eur Polym J*, 2020, **129**, 109621.

15 A. K. Maurya, A. Mishra and N. Mishra, in *Nanoengineered Biomaterials for Advanced Drug Delivery*, Elsevier, 2020, pp. 109–143.

16 S. V. Jermain, C. Brough and R. O. Williams, *Int J Pharm*, DOI:10.1016/j.ijpharm.2017.10.051.

17 I. Ekladious, Y. L. Colson and M. W. Grinstaff, *Nat Rev Drug Discov*, 2019, **18**, 273–294.

18 S. V. Bhujbal, B. Mitra, U. Jain, Y. Gong, A. Agrawal, S. Karki, L. S. Taylor, S. Kumar and Q. (Tony) Zhou, *Acta Pharm Sin B*, 2021, **11**, 2505–2536.

19 X. Ma and R. O. Williams, *J Drug Deliv Sci Technol*, 2019, **50**, 113–124.

20 K. Sarpal, S. Delaney, G. G. Z. Zhang and E. J. Munson, *Mol Pharm*, 2019, **16**, 4836–4851.

21 M. M. Knopp, J. Wendelboe, R. Holm and T. Rades, *European Journal of Pharmaceutics and Biopharmaceutics*, 2018, **130**, 290–295.

22 M. Meere, G. Pontrelli and S. McGinty, *Acta Biomater*, 2019, **94**, 410–424.

23 A. Schittny, J. Huwyler and M. Puchkov, *Drug Deliv*, 2020, **27**, 110–127.

24 D.-G. Yu, J.-J. Li, G. R. Williams and M. Zhao, *Journal of Controlled Release*, 2018, **292**, 91–110.

25 R. Yang, G. G. Z. Zhang, D. Y. Zemlyanov, H. S. Purohit and L. S. Taylor, *J Pharm Sci*, 2023, **112**, 304–317.

26 S. Saboo, P. Bapat, D. Moseson, U. Kestur and L. Taylor, *Pharmaceutics*, 2021, **13**, 735.

27 J. Vijayakumar, N. M. Goudarzi, G. Eeckhaut, K. Schrijnemakers, V. Cnudde and M. N. Boone, *Pharmaceuticals*, 2023, **16**, 733.

28 M. Alhijjaj, S. Yassin, M. Reading, J. A. Zeitler, P. Belton and S. Qi, *Pharm Res*, 2017, **34**, 971–989.

29 J. Li, Y. Wang and D. Yu, *AAPS PharmSciTech*, 2023, **24**, 175.

30 S. Tambe, D. Jain, S. K. Meruva, G. Rongala, A. Juluri, G. Nihalani, H. K. Mamidi, P. K. Nukala and P. K. Bolla, *Pharmaceutics*, 2022, **14**, 2203.

31 T. W. Jarrells and E. J. Munson, *J Pharm Sci*, 2022, **111**, 2765–2778.

32 J. Wu, S. Xu, C. C. Han and G. Yuan, *Journal of Controlled Release*, 2021, **331**, 472–479.

33 S. Qi, S. Roser, K. J. Edler, C. Pigliacelli, M. Rogerson, I. Weuts, F. Van Dycke and S. Stokbroekx, *Pharm Res*, 2013, **30**, 290–302.

34 H. W. Toh, D. W. Y. Toong, J. C. K. Ng, V. Ow, S. Lu, L. P. Tan, P. E. H. Wong, S. Venkatraman, Y. Huang and H. Y. Ang, *Eur Polym J*, 2021, **146**, 110249.

35 N. Asadi, A. R. Del Bakhshayesh, S. Davaran and A. Akbarzadeh, *Mater Chem Phys*, 2020, **242**, 122528.

36 K. R. Zodrow, J. D. Schiffman and M. Elimelech, *Langmuir*, 2012, **28**, 13993–13999.

37 B. Nugraha and L. P. Tan, *J Biomim Biomater Tissue Eng*, 2008, **1**, 69–79.

38 Y. He, R. F. de Araújo Júnior, R. S. Cavalcante, Z. Yu, T. Schomann, Z. Gu, C. Eich and L. J. Cruz, *Biomaterials Advances*, 2023, **145**, 213270.

39 Y. Xue, L. Xu, A. Wang, Y. Ma, W. Zhang, W. Ji, G. Leng, F. Zhou, W. Liu and X. Di, *Journal of Controlled Release*, 2023, **357**, 196–209.

40 T. M. Fahmy, R. M. Samstein, C. C. Harness and W. Mark Saltzman, *Biomaterials*, 2005, **26**, 5727–5736.

41 F. Sun, C. Sui, L. Teng, X. Liu, L. Teng, Q. Meng and Y. Li, *Int J Pharm*, 2010, **397**, 44–49.

42 A. Sokolova, J. Christoforidis, A. Eltobaji, J. Barnes, F. Darmann, A. E. Whitten and L. de Campo, *Neutron News*, 2016, **27**, 9–13.

43 A. Sokolova, A. E. Whitten, L. de Campo, J. Christoforidis, A. Eltobaji, J. Barnes, F. Darmann and A. Berry, *J Appl Crystallogr*, 2019, **52**, 1–12.

44 O. Arnold, J. C. Bilheux, J. M. Borreguero, A. Buts, S. I. Campbell, L. Chapon, M. Doucet, N. Draper, R. Ferraz Leal, M. A. Gigg, V. E. Lynch, A. Markvardsen, D. J. Mikkelson, R. L. Mikkelson, R. Miller, K. Palmen, P. Parker, G. Passos, T. G. Perring, P. F. Peterson, S. Ren, M. A. Reuter, A. T. Savici, J. W. Taylor, R. J. Taylor, R. Tolchenov, W. Zhou and J. Zikovsky, *Nucl Instrum Methods Phys Res A*, 2014, **764**, 156–166.

45 C. Rehm, L. de Campo, A. Brûlé, F. Darmann, F. Bartsch and A. Berry, *J Appl Crystallogr*, 2018, **51**, 1–8.

46 T. Lam, N. Xiong, D. Mannicke and N. Hauser, DOI:10.5281/zenodo.375967.

47 S. R. Kline, *J Appl Crystallogr*, 2006, **39**, 895–900.

48 F. Li, S. R. Parnell, R. Dalgliesh, A. Washington, J. Plomp and R. Pynn, *Sci Rep*, 2019, **9**, 8563.

49 C. Wolf and K. Weigandt, *STFC ISIS Facility*, DOI:10.5286/ISIS.E.RB2220100.

50 J. Ilavsky, *J Appl Crystallogr*, 2012, **45**, 324–328.

51 M. Doucet, J. H. Cho, G. Alina, Z. Attala, J. Bakker, P. Beaucage, W. Bouwman, R. Bourne, P. Butler, I. Cadwallader-Jones, K. Campbell, T. Cooper-Benun, C. Durniak, L. Forster, P. Gilbert, M. Gonzalez, R. Heenan, A. Jackson, S. King, P. Kienzle, J. Krzywon, B. Maranville, N. Martinez, R. Murphy, T. Nielsen, L. O'Driscoll, W. Potrzebowski, S. Prescott, R. Ferraz Leal, P. Rozyczko, T. Snow, A. Washington, L. Wilkins and C. Wolf, *SasView version 5.0.6*, DOI:10.5281/zenodo.7581379.

52 A. Guinier and G. Fournet, *Small-Angle Scattering of X-rays*, John Wiley & Sons, New York, 1955.

53 L. A. Feigin and D. I. Svergun, *Structure Analysis by Small-Angle X-Ray and Neutron Scattering*, Plenum Press, New York, 1987.

54 G. V. Jensen and J. G. Barker, *J Appl Crystallogr*, 2018, **51**, 1455–1466.

55 Y. Chen and Q. Lan, *Int J Biol Macromol*, 2024, **260**, 129459.

56 A. V. Dobrynin and I. Ya. Erukhimovich, *Journal de Physique I*, 1995, **5**, 365–377.

57 R. Andersson, L. F. van Heijkamp, I. M. de Schepper and W. G. Bouwman, *J Appl Crystallogr*, 2008, **41**, 868–885.

58 J. H. Bakker, A. L. Washington, S. R. Parnell, A. A. van Well, C. Pappas and W. G. Bouwman, *Journal of Neutron Research*, 2020, **22**, 57–70.

59 J. Kohlbrecher and A. Studer, *J Appl Crystallogr*, 2017, **50**, 1395–1403.

60 C. Rehm, J. Barker, W. G. Bouwman and R. Pynn, *J Appl Crystallogr*, 2013, **46**, 354–364.

61 H. Furukawa, *Physica A: Statistical Mechanics and its Applications*, 1984, **123**, 497–515.

62 H. Meier and G. R. Strobl, *Macromolecules*, 1987, **20**, 649–654.

63 T. Hashimoto, M. Takenaka and H. Jinnai, *J Appl Crystallogr*, 1991, **24**, 457–466.

Data Availability Statement

Raw SESANS data is available at: https://doi.org/10.5286/ISIS.E.RB2220100. Reduced scattering data is available as supplementary information.